American Mineralogist, Volume 102, pages 632–642, 2017

# Phase relations of $MgFe_2O_4$ at conditions of the deep upper mantle and transition zone

LAURA UENVER-THIELE[1,*], ALAN B. WOODLAND[1], TIZIANA BOFFA BALLARAN[2], NOBUYOSHI MIYAJIMA[2], AND DAN J. FROST[2]

[1]Institut für Geowissenschaften, Goethe-Universität Frankfurt, Altenhöferallee 1, D-60438, Frankfurt am Main, Germany
[2]Bayerisches Geoinstitut, Universität Bayreuth, D-95440 Bayreuth, Germany

## ABSTRACT

Phase relations of magnesioferrite ($MgFe_2O_4$) have been studied between 8 and 18 GPa and 1000–1600 °C using multi-anvil experiments. At 8–10 GPa and 900–1200 °C, $MgFe_2O_4$ breaks down to $Fe_2O_3$+MgO. At higher temperatures, a new phase appears along with $Fe_2O_3$. Although this new phase is unquenchable, EPMA and TEM data point to a composition with $Mg_5Fe_2O_8$ or $Mg_4Fe_2O_7$ stoichiometry. Depending on pressure and temperature, other stoichiometries also appear to be stable together with $Fe_2O_3$. In terms of pressure, the stability field of the unquenchable phases + hematite widens with increasing temperature to 3 ± 1 GPa at ~1400 °C, and then narrows to ~1 GPa at 1600 °C. The recoverable assemblage of $Mg_2Fe_2O_5$+$Fe_2O_3$ becomes stable between 11–13 GPa. The $Mg_2Fe_2O_5$+$Fe_2O_3$ assemblage is stable up to at least 18 GPa at 1300 °C without any evidence of a hp-$MgFe_2O_4$ phase. In addition, hematite plays an important role in the phase relations of $MgFe_2O_4$ by being present over a wide range in pressure and temperature together with a Mg-rich Fe-oxide. Interestingly, hematite incorporates variable amounts of Mg whereby its concentration appears to be a function of temperature. This experimental study has implications for interpreting inclusions in natural diamonds where magnesioferrite occurs by placing a maximum pressure stability on the formation of this phase. Through these inclusions, it also provides constraints on diamond formation and their subsequent evolution prior to eruption. For example, the occasional observation of nano-sized magnesioferrite within (Mg,Fe)O inclusions must have either formed from a high-pressure precursor phase with a different stoichiometry at transition zone or upper lower mantle conditions, or it exsolved directly from the host (Mg,Fe)O under upper mantle conditions (i.e., <9–10 GPa). Since several studies report various non-silicate inclusions with simple oxide compositions, including magnesioferrite, magnetite, or ferropericlase, such inclusions provide evidence for variable redox conditions at the time of entrapment.

**Keywords:** Magnesioferrite, $MgFe_2O_4$, $Mg_2Fe_2O_5$, deep upper mantle, transition zone, high pressure

## INTRODUCTION

Spinel structured minerals with the chemical formula $AB_2O_4$ are of particular interest in having the ability to incorporate ferric ($Fe^{3+}$) and ferrous ($Fe^{2+}$) cations into their structure, which makes their stability sensitive to redox conditions. Such phases commonly occur in the peridotitic upper mantle and transition zone. Magnesioferrite ($MgFe_2^{3+}O_4$) is an example of such $Fe^{3+}$-bearing end-member components that may be stable at such high pressure and temperature conditions. $MgFe_2O_4$ exhibits a cubic crystal structure (space group $Fd\bar{3}m$) with one tetrahedral and two octahedral sites per $AB_2O_4$ formula unit.

The high-pressure behavior of several spinel group minerals has been experimentally investigated over the last few decades, with a main interest being the nature of the "post-spinel" phase at conditions of the deep upper mantle and transition zone (e.g., Huang and Bassett 1986; Akaogi et al. 1999; Wang et al. 2003; Levy et al. 2004; Schollenbruch et al. 2010; Woodland et al. 2012; Ono et al. 2006; Kyono et al. 2012; Enomoto et al. 2009; Ishii et al. 2014, 2015). Apart from experimental studies, mineral inclusions in diamonds brought up to the surface provide a direct window into the Earth's interior. Thus, minerals entrapped by diamond represent a local part of the Earth's mantle. But interpreting the chemical signatures of these minerals can be hampered by fractures in diamond, which allows metasomatic interactions and/or changes in redox state. Additionally, high-pressure and high-temperature phases can also decompose during upwelling.

With regard to spinel group minerals, it has been reported that they transform into denser orthorhombic structures of $CaFe_2O_4$ (*Pnma*), $CaTi_2O_4$ (*Cmcm*), or $CaMn_2O_4$ (*Pbcm*) type at high pressures (e.g., Andrault and Bolfan-Casanova 2001; Yamanaka et al. 2008) or disproportionate. For example, at ~10 GPa and 700–1400 °C magnetite ($FeFe_2O_4$) breaks down to $Fe_4O_5$+$Fe_2O_3$ (Woodland et al. 2012), while hercynite ($FeAl_2O_4$) and spinel ($MgAl_2O_4$) decompose into their constituent oxides (Schollenbruch et al. 2010; Akaogi et al. 1999). Andrault and Bolfan-Casanova (2001) studied magnesioferrite by in situ X-ray diffraction at high pressures (>20 GPa) using YAG laser annealing in a diamond-anvil cell and reported a phase transformation at ~25 GPa, apparently to a $CaMn_2O_4$-type polymorph. Combining their *P-V-T* data on magnesioferrite with available thermodynamic data, Levy et al. (2004) proposed a phase diagram for

* E-mail: Uenver-Thiele@em.uni-frankfurt.de

0003-004X/17/0003–632$05.00/DOI: http://dx.doi.org/10.2138/am-2017-5871

$MgFe_2O_4$ that included a large stability field of MgO+$Fe_2O_3$ at intermediate pressure and temperature conditions, together with an assumed field of a hp-$MgFe_2O_4$ phase at $P > 17$ GPa. However, Levy et al. (2004) never produced the hp-$MgFe_2O_4$ phase and they had no direct experimental evidence for the existence of a MgO+$Fe_2O_3$ stability field at room temperature even up to 35 GPa.

In natural samples, magnesioferrite has been identified in ferropericlase inclusions occurring in diamond (Harte et al. 1999; Wirth et al. 2014). From their TEM observations, Wirth et al. (2014) suggested that the magnesioferrite might have previously been a hp-$MgFe_2O_4$ phase, formed by exsolution from an $Fe^{3+}$-bearing (Mg,Fe)O host during decompression enroute from the lower mantle. However, such an interpretation depends on the high-pressure phase relations of $MgFe_2O_4$, which are currently only poorly constrained as just described.

The discovery of new oxides with $M_4O_5$ stoichiometry (Enomoto et al. 2009; Lavina et al. 2011; Woodland et al. 2012; Ishii et al. 2014, 2015; Myhill et al. 2016) opens the possibility that analogous behavior may occur in the Mg-$Fe^{3+}$-system. In fact, complete substitution of Mg into $Fe_4O_5$, producing the new oxide phase $Mg_2Fe_2O_5$ has been recently reported (Boffa Ballaran et al. 2015). This phase exhibits the $CaFe_3O_5$-type structure (Boffa Ballaran et al. 2015). Considering the phase relations of other simple oxides, the stability of $Mg_2Fe_2O_5$ may also have implications for the $MgFe_2O_4$ system. Thus, our experimental study aims to investigate the phase relations of magnesioferrite at high pressures and high temperatures to: (1) identify the conditions for the breakdown of magnesioferrite; (2) verify the stability of a possible hp-$MgFe_2O_4$ phase; and (3) to assess whether $Mg_2Fe_2O_5$ is relevant to the $MgFe_2O_4$ bulk composition. Considering the occurrence of magnesioferrite in diamonds (e.g., Harte et al. 1999; Wirth et al. 2014), we then go on to briefly discuss the implications of our results for the Earth's upper mantle and transition zone.

## Experimental methods

### Starting materials

Stoichiometric mixtures of $Fe_2O_3$ and MgO or pre-synthesized magnesioferrite were used for high-pressure experiments (Table 1). $Fe_2O_3$ and MgO were pre-sintered in air at 1000 °C. For synthesizing $MgFe_2O_4$ a stoichiometric mixture of $Fe_2O_3$ and MgO was ground together and pressed into pellets and sintered in air in a muffle furnace (at 1 atm) at 1000 °C for 40 h. After regrinding and repressing into pellets, the sample was sintered again at 1000 °C for 24 h, then at 950 °C (24 h), followed by a final cycle at 900 °C (24 h). The sample was then removed from the furnace and allowed to cool to room temperature. The resulting product was fine grained and had a light reddish-brown color. Several fragments were analyzed by electron microprobe (EPMA) to verify homogeneity and composition. X-ray powder diffraction revealed virtually pure magnesioferrite with a unit-cell parameter of $a_o = 8.3875(1)$ Å with only a minor trace of $Fe_2O_3$. Comparing with the results of O'Neill et al. (1992), this unit-cell parameter indicates a stoichiometric composition with a degree of inversion of x = 0.84.

### Experimental procedures

High pressure-temperature experiments were performed at the University of Frankfurt and the Bayerisches Geoinstitut, Bayreuth over a *P-T* range of 8–18 GPa

**Table 1.** Experimental conditions and run products, including unit-cell parameters of magnesioferrite

| Experiment | Starting material | Pressure (GPa) | Temperature (°C) | Run duration (h) | Run products | Unit-cell parameter of $MgFe_2O_4$ (Å) |
|---|---|---|---|---|---|---|
| M573 | MgO+$Fe_2O_3$ | 8 | 900 | 20 | per + hem | – |
| M585 | 10% $MgFe_2O_4$ + 90% MgO + $Fe_2O_3$ | 8 | 900 | 24 | per + hem | – |
| M518 | $MgFe_2O_4$ | 8 | 1100 | 5.5 | mf | 8.3808(1) |
| M517 | $MgFe_2O_4$ | 8 | 1300 | 5.5 | mf | 8.3826(2) |
| M592 | 10% $MgFe_2O_4$ + 90% MgO + $Fe_2O_3$ | 8 | 1500 | 2 | mf | 8.3810(4) |
| M577 | $MgFe_2O_4$ | 9 | 900 | 24 | per + hem | – |
| M593 | 10% $MgFe_2O_4$ + 90% MgO + $Fe_2O_3$ | 9 | 1000 | 18 | per + hem | – |
| V862o | MgO + $Fe_2O_3$ | 9 | 1100 | 5.5 | mf | 8.3824(2) |
| V862u | $MgFe_2O_4$ | 9 | 1100 | 5.5 | mf | 8.3799(1) |
| V864o | $MgFe_2O_4$ | 9 | 1300 | 4.5 | mf | 8.3814(0) |
| V864u | MgO + $Fe_2O_3$ | 9 | 1300 | 4.5 | mf | 8.3812(2) |
| V865o | MgO + $Fe_2O_3$ | 9 | 1300 | 1.5 | mf | 8.3820(0) |
| V865u | $MgFe_2O_4$ | 9 | 1300 | 1.5 | mf | 8.3812(2) |
| M594 | 10% $MgFe_2O_4$ + 90% MgO + $Fe_2O_3$ | 9 | 1500 | 3 | mf | 8.3807(2) |
| M569 | $MgFe_2O_4$ | 10 | 1000 | 17 | per + hem | – |
| M588 | 10% $MgFe_2O_4$ + 90% MgO + $Fe_2O_3$ | 10 | 1200 | 5 | per + hem | – |
| V841o | MgO + $Fe_2O_3$ | 10 | 1300 | 5.5 | UQ-$O_7$ + UQ-$O_8$ + hem | – |
| M553 | 2MgO + $Fe_2O_3$ | 10 | 1400 | 4 | UQ-$O_7$ + hem | – |
| M629 | $MgFe_2O_4$ | 10 | 1500 | 3 | mf + hem + UQ-$O_6$ + (mgs) | – |
| M633 | $MgFe_2O_4$ | 10 | 1600 | 1.5 | mf + UQ-$O_6$ | 8.3794(7) |
| M632 | $MgFe_2O_4$ | 11 | 1300 | 4.5 | hem + UQ-$O_{14}$ | – |
| M631 | $MgFe_2O_4$ | 11 | 1450 | 4 | hem + UQ-$O_8$ | – |
| M616 | $MgFe_2O_4$ | 11 | 1600 | 2 | $O_5$ + hem | – |
| M630 | $MgFe_2O_4$ | 12 | 1350 | 4 | hem + UQ-$O_{14}$ | – |
| M568 | MgO + $MgFe_2O_4$ | 12 | 1400 | 5 | UQ-$O_8$ + hem | – |
| M583 | $MgFe_2O_4$ | 12 | 1500 | 4 | UQ-$O_7$ + $O_5$ + hem | – |
| M590 | $MgFe_2O_4$ | 13 | 1200 | 4 | per + hem | – |
| M617 | $MgFe_2O_4$ | 13 | 1400 | 5.5 | $O_5$ + hem + UQ-$O_9$ | – |
| M551 | 2MgO + $Fe_2O_3$ | 13 | 1500 | 3.5 | UQ-$O_7$ + hem | – |
| Z1463o | $MgFe_2O_4$ | 14 | 1400 | 3 | $O_5$ + hem | – |
| Z1461o | $MgFe_2O_4$ | 16 | 1300 | 3 | per + hem + $O_5$ | – |
| H4084 | MgO + $MgFe_2O_4$ | 18 | 1200 | 4.5 | per + hem | – |
| H3889 | $MgFe_2O_4$ | 18 | 1300 | 5.5 | $O_5$ + hem + (mgs) | – |

*Notes:* Run product abbreviations: per = periclase; hem = hematite; mf = magnesioferrite; (mgs) = traces of magnesite; $O_5 = Mg_2Fe_2O_5$; UQ-$O_6$ = unquenchable phase with a stoichiometry of $Mg_3Fe_2O_6$; UQ-$O_7$ = unquenchable phase with a stoichiometry of $Mg_4Fe_2O_7$; UQ-$O_8$ = unquenchable phase with a stoichiometry of $Mg_5Fe_2O_8$; UQ-$O_9$ = unquenchable phase with a stoichiometry of $Mg_6Fe_2O_9$; UQ-$O_{14}$ = unquenchable phase with a stoichiometry of $Mg_{11}Fe_2O_{14}$.

and 900–1600 °C (see Table 1). Individual run conditions are presented in Table 1. The experiments performed at the University of Frankfurt were conducted in an 800t Walker-type multi-anvil apparatus (Walker et al. 1990) giving maximum load pressure of 14 GPa. Pressure calibration as well as the cell assembly design are described in detail by Brey et al. (2008). Experiments carried out at the Bayerisches Geoinstitut Bayreuth were performed using 500t, 1000t, and 5000t multi-anvil presses. The pressure calibration and setup of those multi-anvil presses are reported in Keppler and Frost (2005). The assembly at the University of Frankfurt uses Re-foil as a heater, while $LaCrO_3$ is employed as heater at the Bayerisches Geoinstitut. The temperature was monitored by $W_3/Re_{97}$–$W_{25}/Re_{75}$ thermocouples with the electromotive force uncorrected for pressure. Uncertainties in pressure and temperature are ±0.5 GPa and ±30–50 °C, respectively (Keppler and Frost 2005).

Sample powders were packed into capsules made from Pt foil, along with a small amount of $PtO_2$ placed at the bottom and/or the top of the capsule to keep the oxygen fugacity ($f_{O_2}$) high during the experiment. At such a high $f_{O_2}$, Fe-loss to Pt metal is negligible. Pieces of Pt-foil were placed between the starting material and the $PtO_2$ to minimize direct contact. In earlier experiments, we found that Pt can be locally incorporated in our oxide phases, when $PtO_2$ was in direct contact with our starting materials. In some experiments two capsules could be employed, allowing the simultaneous use of two different starting materials to directly monitor reaction direction (see Table 1).

Experiments followed the standard procedure of cold pressurizing, with subsequent heating to the desired temperature at a rate of ~50 °C/min. Isobaric quenching of the experiments was achieved by turning off the power to the furnace, after which the sample was decompressed. The cooling rate was ~200–250 °C/s.

### Sample characterization

Run products were analyzed by EPMA, powder X-ray diffraction and/or transmission electron microscopy (TEM). A few fragments of each sample were mounted in epoxy, polished and carbon coated for microprobe analysis. Measurements were carried out with a five-spectrometer JEOL JXA-8900 superprobe at the University of Frankfurt. Pure MgO, $Fe_2O_3$, and Pt metal were employed as primary standards. A CITZAF algorithm was used for matrix correction (Armstrong 1993). Measurements were performed in wavelength-dispersive mode using 15 kV accelerating voltage, a beam current of 20 nA and a beam spot size of 1 μm. Integration times for Fe and Pt were 40 s on the peak and 20 s on background. An integration time of 40 s on the peak and background was adjusted for Mg. Backscattered electron images were taken to investigate microtextures and to verify homogeneity of the mineral grains. If the grains were large enough (>20 μm), 3–5 points were measured on a single grain.

Further phase identification was performed with X-ray powder diffraction patterns that were collected on two diffractometers. One was a Philips X'Pert PRO diffractometer at the Bayerisches Geoinstitut, Bayreuth using monochromatic Co$K\alpha$ ($\lambda$ = 1.78897 Å) radiation selected with a focusing monochromator, a symmetrically cut curved Johansson Ge (111) crystal and equipped with a Philips X'celerator detector. Silicon (NIST SRM 640c) was added as an internal standard. Data were collected between 10° and 120° 2θ at 40 kV and 40 mA. Other patterns were collected with a STOE Stadi P diffractometer at the University of Frankfurt operating at 45 kV and 35 mA and using monochromatic Mo$K\alpha$ ($\lambda$ = 0.70926 Å) radiation, along with a linear PSD or a Mythen detector. In this later case, the sample material containing a Si internal standard (cross-calibrated with the standard in Bayreuth) was mounted in a 0.5 mm diameter capillary and measured in transmission mode between 1–100° 2θ. Unit-cell parameters were determined from full-pattern Rietveld refinements using the general structure analysis system (GSAS; Larson and von Dreele 1994) software package and the EXPGUI interface of Toby (2001).

TEM analysis was carried out using FEI Titan G2 80-200 S/TEM equipped with 4 SDD energy-dispersive X-ray spectrometers, operated at 200 kV. One of the recovered samples (M568) was cut and polished to make a thin section. The thin section was mounted on a Mo grid and Ar-ion milled to electron transparency at accelerating voltages of 4.0 kV with an incident angle of 8° using a precision ion polishing system (Gatan, model 691). The sample foil was coated with amorphous carbon to reduce charging.

## Results and discussion

The use of different starting mixtures permitted us to demonstrate the direction of reaction and, thus, to determine the stable phase assemblage at the conditions of a given experiment (Table 1). Broadly using the proposed phase diagram of Levy et al. (2004), we employed either $MgFe_2O_4$ or stoichiometric mixtures of $MgO+Fe_2O_3$ to unequivocally demonstrate which assemblage was stable at a given pressure and temperature. In several cases, two separate capsules with different starting materials were included in a single experiment. In other cases, 10% $MgFe_2O_4$ was mixed together with $MgO+Fe_2O_3$ to minimize potential kinetic problems related to nucleation of magnesioferrite from an oxide mixture. The direction of reaction could then be monitored from the relative phase proportions determined from refinement of the X-ray diffraction pattern.

Depending on the pressure and temperature of the experiment, the duration varied from 1.5–24 h (see Table 1). Backscattered electron imaging of the run products confirms significant grain growth and essentially complete recrystallization. Most samples revealed homogenous and well-crystalized grains, whereas several experiments (e.g., M553, M568, V841o; Table 1) contained grains that exhibited extremely fine-grained internal textures, suggesting reaction had occurred during quenching (see below). Stoichiometric calculations based upon microprobe analyses indicate that, with the help of a little $PtO_2$, the oxygen fugacity had been kept high enough so that the iron remained in the ferric state for the duration of the experiments. At such oxidizing conditions, incorporation of Pt into the oxide phases needed to be monitored, as hematite with up to ~7 wt% $PtO_2$ or $MgFe_2O_4$ with up to 1 wt% were observed in a few samples, for crystals in direct contact with $PtO_2$. Such samples were not considered when assessing the phase relations of $MgFe_2O_4$. No measureable or only traces of Pt were observed in either ferropericlase or the new $Mg_2Fe_2O_5$ phase (Table 2). Magnesite appeared in trace quantities in several samples (see Tables 1 and 2). This was possibly introduced into the experiments as adsorbed $CO_2$ on the $PtO_2$ powder, which has a very fine grain size. Although the presence of magnesite alters the bulk composition, the small amounts should have negligible effect on the stability of the coexisting oxide phases.

### The breakdown of $MgFe_2O_4$ at low temperatures

At 8–10 GPa and temperatures of 900–1200 °C $MgFe_2O_4$ was observed to breakdown to its constituent oxide phases according to the reaction:

$$\underset{\text{mf}}{MgFe_2O_4} = \underset{\text{per}}{MgO} + \underset{\text{hem}}{Fe_2O_3}. \quad (1)$$

Backscatter electron images reveal that where magnesioferrite was stable, it produced grains up to 150 μm in size, whereas mixtures of MgO and $Fe_2O_3$ were much finer grained (~10 μm, compare Figs. 1a and 1b). The measured cell parameter for periclase in our experiments agrees with the value of $a_o$ = 4.2110 Å reported for MgO by Hazen (1976) (Table 3). The position of the phase boundary can be described by the following equation (see Fig. 2):

$$P\,(\text{GPa}) = 6.7 \times 10^{-3} \times T\,(°\text{C}) + 1.8.$$

The boundary computed by Levy et al. (2004) lies at significantly higher pressures. On the other hand, the database of Holland and Powell (2011) seems to reproduce our results reasonably well, even if their slope is much steeper than that implied from our data.

**TABLE 2.** Representative electron microprobe data (in wt%) of experimental run products

| Sample | | H3889 | H3889 | H3889 | M517 | M518 | M551 | M551 | M553 | M553 | M568 | M568 | M568 | M568 |
|---|---|---|---|---|---|---|---|---|---|---|---|---|---|---|
| MgO | | 2.99 | 48.54 | 32.28 | 21.22 | 22.17 | 50.53 | 3.49 | 2.82 | 49.61 | 55.87 | 56.39 | 2.39 | 2.42 |
| FeO | | 85.95 | 1.33 | 62.39 | 72.49 | 71.41 | 44.58 | 86.24 | 86.5 | 45.53 | 41.56 | 41.33 | 87.43 | 87.79 |
| $PtO_2$ | | b.d.l. | 0.05 | 0.13 | b.d.l. | 0.21 | b.d.l. | b.d.l. | b.d.l. | b.d.l. | b.d.l. | b.d.l. | 0.03 | 0.02 | b.d.l. |
| Totals | | 88.94 | 49.92 | 94.80 | 93.71 | 93.79 | 95.11 | 89.73 | 89.32 | 95.14 | 97.43 | 97.75 | 89.84 | 90.21 |
| comment | | hem | mgs | $Mg_2Fe_2O_5$ | mf | mf | UQ-$O_7$ | hem | hem | UQ-$O_7$ | UQ-$O_8$ | UQ-$O_8$ | hem | hem |

| Sample | M569 | M569 | M573 | M577 | M577 | M583 | M583 | M583 | M588 | M590 | M592 | M592 | M594 |
|---|---|---|---|---|---|---|---|---|---|---|---|---|---|
| MgO | 0.66 | 99.55 | 0.61 | 0.45 | 99.87 | 50.54 | 2.94 | 33.56 | 1.45 | 1.67 | 21.72 | 21.55 | 21.01 |
| FeO | 89.18 | 1.94 | 89.04 | 89.90 | 1.76 | 46.97 | 87.82 | 63.52 | 89.00 | 88.83 | 72.78 | 72.58 | 72.41 |
| $PtO_2$ | b.d.l. | b.d.l. | 0.11 | b.d.l. | b.d.l. | b.d.l. | b.d.l. | b.d.l. | b.d.l. | b.d.l. | b.d.l. | 0.03 | b.d.l. |
| Totals | 89.84 | 101.49 | 89.76 | 90.35 | 101.63 | 97.51 | 90.76 | 97.08 | 90.45 | 90.50 | 94.50 | 94.16 | 93.42 |
| comment | hem | MgO | hem | hem | MgO | UQ-$O_7$ | hem | $Mg_2Fe_2O_5$ | hem | hem | mf | mf | mf |

| Sample | M594 | M616 | M616 | M617 | M617 | M617 | M629 | M629 | M629 | M629 | M630 | M631 |
|---|---|---|---|---|---|---|---|---|---|---|---|---|
| MgO | 21.05 | 3.04 | 32.95 | 2.09 | 33.61 | 61.86 | 21.64 | 2.92 | 48.40 | 45.11 | 76.59 | 55.30 |
| FeO | 72.76 | 86.12 | 63.05 | 87.69 | 62.70 | 36.39 | 73.38 | 88.29 | 1.32 | 51.24 | 24.01 | 41.02 |
| $PtO_2$ | 0.01 | b.d.l. | b.d.l. | b.d.l. | b.d.l. | b.d.l. | 0.06 | b.d.l. | b.d.l. | 0.05 | b.d.l. | b.d.l. |
| Totals | 93.82 | 89.16 | 96.00 | 89.78 | 96.31 | 98.25 | 95.08 | 91.21 | 49.72 | 96.40 | 100.60 | 96.32 |
| comment | mf | hem | $Mg_2Fe_2O_5$ | hem | $Mg_2Fe_2O_5$ | UQ-$O_9$ | mf | hem | mgs | UQ-$O_6$ | UQ-$O_{14}$ | UQ-$O_8$ |

| Sample | M631 | M632 | M633 | M633 | V841o | V841o | V841o | V841o | V862o | V862o | V862u | V864o |
|---|---|---|---|---|---|---|---|---|---|---|---|---|
| MgO | 2.19 | 75.87 | 44.67 | 21.17 | 50.49 | 49.17 | 2.49 | 54.83 | 22.51 | 22.49 | 21.84 | 21.95 |
| FeO | 87.98 | 24.05 | 49.22 | 70.74 | 44.73 | 1.72 | 87.39 | 41.54 | 71.59 | 72.23 | 71.20 | 72.45 |
| $PtO_2$ | b.d.l. | 0.08 | 0.25 | 0.03 | n.a. | n.a. | n.a. | n.a. | 0.02 | b.d.l. | b.d.l. | b.d.l. |
| Totals | 90.17 | 100.00 | 94.14 | 91.94 | 95.22 | 50.89 | 89.88 | 96.37 | 94.12 | 94.72 | 93.04 | 94.40 |
| comment | hem | UQ-$O_{14}$ | UQ-$O_6$ | mf | UQ-$O_7$ | mgs | hem | UQ-$O_8$ | mf | mf | mf | mf |

| Sample | V864u | V865u | V865o | Z1461o | Z1461o | Z1463o | Z1463o |
|---|---|---|---|---|---|---|---|
| MgO | 21.77 | 22.14 | 21.69 | 1.59 | 32.34 | 32.54 | 2.67 |
| FeO | 72.13 | 71.16 | 70.93 | 89.88 | 64.77 | 64.17 | 88.29 |
| $PtO_2$ | b.d.l. | n.a. | n.a. | b.d.l. | b.d.l. | b.d.l. | b.d.l. |
| Totals | 93.90 | 93.30 | 92.62 | 91.47 | 97.11 | 96.71 | 90.96 |
| comment | mf | mf | mf | hem | $Mg_2Fe_2O_5$ | $Mg_2Fe_2O_5$ | hem |

*Notes*: Abbreviations as in Table 1. b.d.l. = below detection limit; n.a. = not analyzed.

### $MgFe_2O_4$ breakdown at higher temperature

At temperatures >1200 °C and 9–10 GPa, $MgFe_2O_4$ no longer breaks down directly to MgO+$Fe_2O_3$. Although the powder diffraction patterns often contain peaks consistent with hematite, MgO, and $MgFe_2O_4$, the peaks are broad and difficult to refine, suggesting that these phases are poorly crystalline or of extremely fine grain size. Furthermore, there are additional diffraction peaks that do not belong to any of these phases. In these cases, estimated phase proportions of MgO and $Fe_2O_3$ are significantly different from those observed in the lower temperature experiments. Following the phase diagram of Levy et al. (2004), a transformation to hp-$MgFe_2O_4$ would be expected. However, neither our microprobe analyses nor our powder diffraction patterns are consistent with a high-pressure polymorph being present. The orthorhombic structures frequently encountered in post-spinel transitions (i.e., the $CaFe_2O_4$, $CaTi_2O_4$, and $CaMn_2O_4$-type structures), tetragonally distorted structures (e.g., Yong et al. 2012; Kyono et al. 2012) proved to be inconsistent with our data. The diffraction peaks also cannot be fitted with the $Mg_2Fe_2O_5$ structure (Boffa Ballaran et al. 2015). Nevertheless, XRD patterns and microprobe analyses of the run products confirm the breakdown of $MgFe_2O_4$ at pressures of ~9–10 ±0.5 GPa and temperatures >1200 °C (Tables 1 and 2; Fig. 3).

An important characteristic of the run products in this pressure-temperature range is their texture, as revealed by BSE-imaging. They are marked by the presence of coarse-grained hematite coexisting with another phase that clearly has a much lower mean atomic number (Fig. 4a). The presence of well-developed triple junctions provides textural evidence for equilibrium conditions in these experiments (Figs. 4a and 4b). In many cases, the additional phase can also be quite coarse-grained (>100 μm; Fig. 4b), even though the grains themselves have a very fine internal structure (Figs. 4b and 4c). Thus, it appears that this phase has decomposed or at least partially decomposed either during temperature quenching or decompression. The coexistence of hematite in the experiments indicates that this phase must have been substantially richer in Mg than the $MgFe_2O_4$ starting composition. We can rule out $Mg_2Fe_2O_5$ since it is known to be recoverable from 15 GPa and ~1550 °C and there is no reason to suspect that its behavior should be different at somewhat lower pressures (Boffa Ballaran et al. 2015). In spite of its unquenchable nature, the resultant very fine grain size of the mixture (<<1 μm and see below) means that microprobe analyses average over a significant volume and can give an indication of the composition of the original phase. In fact, for a given sample multiple microprobe analyses yield consistent compositions, reproducible within ±1–2 wt%. For example, compositions of 50.5 wt% MgO and 44.6 wt% FeO

**TABLE 3.** Unit-cell parameters of MgO

| Sample | *a* (Å) | *V* (Å$^3$) |
|---|---|---|
| M569 | 4.2120(1) | 74.726(6) |
| M573 | 4.2120(2) | 74.72(1) |
| M577 | 4.2118(1) | 74.714(7) |
| M585 | 4.2119(8) | 74.72(4) |
| M588 | 4.2109(1) | 74.666(6) |
| M590 | 4.2112(2) | 74.683(9) |
| M593 | 4.2118(2) | 74.716(10) |
| H4084 | 4.2120(1) | 74.724(4) |

*Note:* Uncertainties in parentheses are those returned by the GSAS refinement.

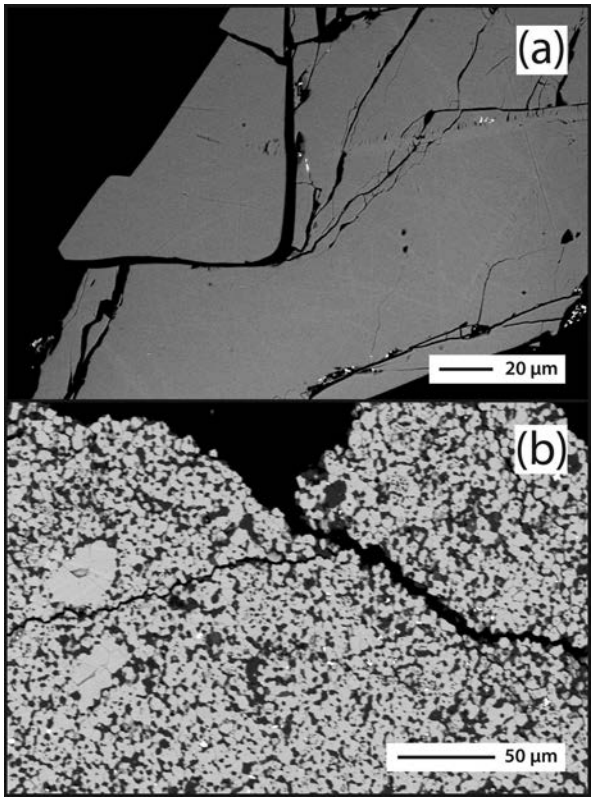


**FIGURE 1.** BSE image of (**a**) a large crystal of $Mg_2Fe_2O_5$ [experiment H3975; crystal structure published in Boffa Ballaran et al. (2015)] in comparison with (**b**) fine-grained $Fe_2O_3$+MgO (experiment M569).

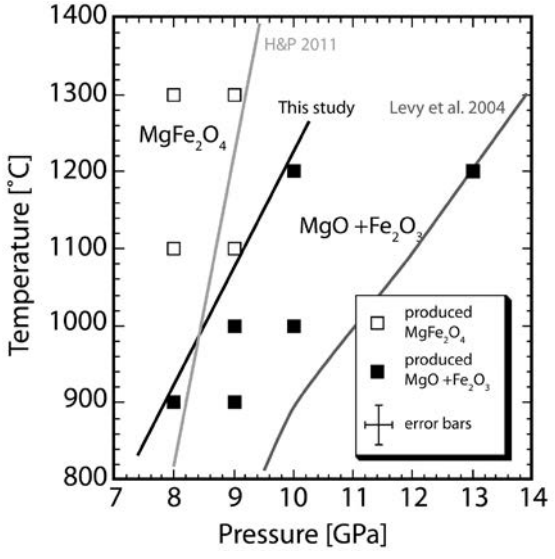


**FIGURE 2.** Position of the boundary between $MgFe_2O_4$ and the $MgO+Fe_2O_3$ phase fields as a function of pressure and temperature. The phase boundary of Levy et al. (2004) and that calculated from the Holland and Powell (2011) database are plotted for comparison. All symbols are experiments from this study. A representative error bar in terms of pressure and temperature is given in the legend for reference.

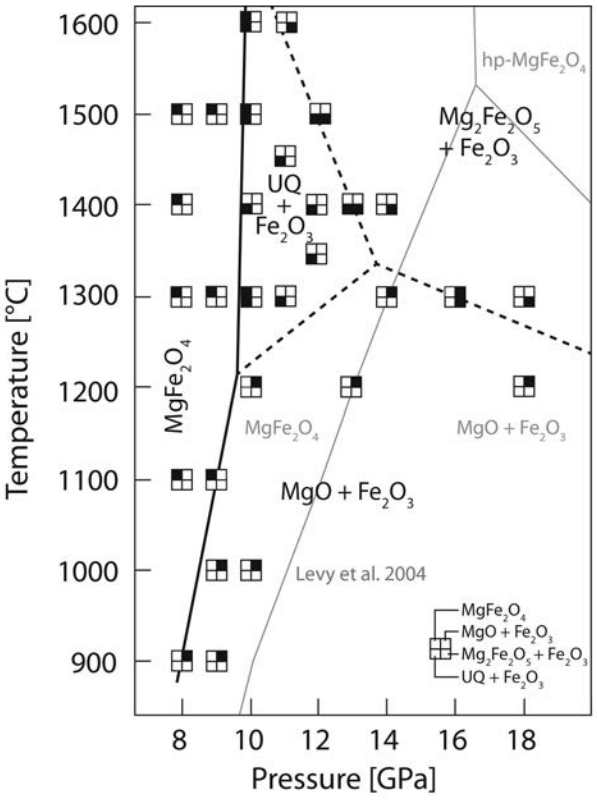


**FIGURE 3.** Phase diagram for magnesioferrite between 8–18 GPa and 900–1600 °C. Errors in pressure and temperature are 0.5 GPa and ±30–50 °C, respectively (Keppler and Frost 2005). Also shown in gray are the phase boundaries proposed by Levy et al. (2004). Above 1200 °C, magnesioferrite breaks down to $Fe_2O_3$ and an unquenchable, Mg-rich phase. At higher pressures (≥14 GPa) the assemblage $Mg_2Fe_2O_5$+$Fe_2O_3$ becomes stable (see text). UQ = unquenchable phase.

(sample M551) and 55.9 wt% MgO and 41.6 wt% FeO (sample M568) suggest stoichiometries for the unquenchable phase of $Mg_4Fe_2O_7$ and $Mg_5Fe_2O_8$, respectively, when charge balance is assumed (Table 4). This assessment also indicates that Fe was maintained in the ferric state during the experiments through the presence of the $PtO_2$. These derived compositions are also inconsistent with the $Mg_2Fe_2O_5$ stoichiometry (Table 4).

Sample M568 was investigated by TEM to obtain additional compositional and textural information about the unquenchable phase. Dark-field images reveal a vermicular intergrowth of two phases at the scale of ~10 nm consistent with spinodal decomposition as suspected from the BSE images (Fig. 5a). STEM-EDX chemical mapping yields two distinct chemical domains: a Fe-rich domain with a composition corresponding to $MgFe_2O_4$ and a Fe-poor domain, much richer in Mg (Fig. 5a, inset). Electron diffraction patterns made by fast Fourier transforms (FFT) in the HRTEM (Fig. 5b) of the Fe-rich domains confirm a cubic spinel structure (Fig. 5c) consistent with the measured $MgFe_2O_4$ composition, while the Mg-rich domains exhibit a rock salt structure, as expected for MgO (Fig. 5d). Results of chemical mapping over the large area yield a bulk composition of $Mg_5Fe_2O_8$, which agrees with the microprobe measurement for this sample (Tables 2 and 4).

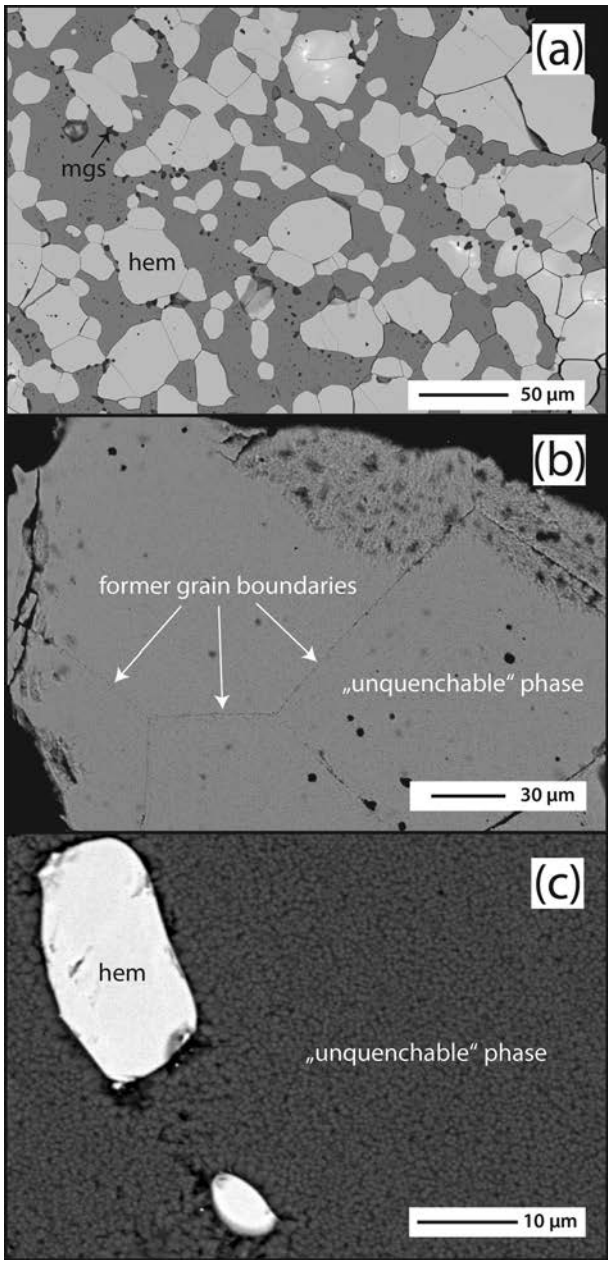


**Figure 4.** (**a**) Backscatter image of sample V841o exhibiting large crystals of hematite surrounded by the unquenchable phase with mottled texture. (**b**) Experiment M553 exhibits the "unquenchable" phase. Grain boundaries of larger crystals with triple junctions can be observed indicating equilibrium conditions at given pressure and temperature of the experiment. Abbreviations: hem = hematite, mgs = magnesite. (**c**) Backscatter image of sample M551 illustrating the texture of the "unquenchable" phase, which decomposed to MgO and $Fe_2O_3$.

Since we cannot definitively identify the structure and composition of this Mg-rich phase or phases stable at high temperatures and pressures, we informally refer to it as an "unquenchable" phase (UQ). Thus, we propose that $MgFe_2O_4$ breaks down to an assemblage of hematite and an unquenchable Mg-Fe oxide with an original stoichiometry of, e.g., $Mg_4Fe_2O_7$ or $Mg_5Fe_2O_8$,

**Table 4.** Possible Fe-Mg oxide stoichiometries matched with their expected compositions as measured by bulk microprobe analysis

| EPMA analysis (wt%) | | Possible stoichiometry |
|---|---|---|
| FeO | MgO | |
| 72(1) | 21(1) | $MgFe^{3+}_2O_4$ |
| 63(1) | 33(1) | $Mg_2Fe^{3+}_2O_5$ |
| 51(1) | 44(1) | $Mg_3Fe^{3+}_2O_6$ |
| 46(1) | 50(1) | $Mg_4Fe^{3+}_2O_7$ |
| 41(1) | 56(1) | $Mg_5Fe^{3+}_2O_8$ |
| 36(1) | 61(1) | $Mg_6Fe^{3+}_2O_9$ |
| 24(1) | 76(1) | $Mg_{11}Fe^{3+}_2O_{14}$ |

depending on the exact pressure and temperature of the experiment. In our phase diagram, we have chosen to lump this region together into a single field, even though in detail more than one Mg-rich phase may be stable in this region (Fig. 3). In fact, various hypothetical compositions can be considered that can be matched up with observed bulk microprobe analyses (Table 4; Figs. 6 and 7). The coexistence of a particular phase stoichiometry with hematite requires that all other phases lying in between are unstable at the given pressure and temperature. Two experiments (M630, M632; Table 1) also exhibit an unquenchable phase coexisting with hematite, but yield a composition anomalously high in Mg (i.e., ~76 wt% MgO and ~24 wt% FeO; Table 2). This composition would imply a $Mg_{11}Fe_2O_{14}$ stoichiometry and is consistent with the qualitatively higher proportion of coexisting hematite in these samples compared with those containing other unquenchable phases. Considering the distribution of the different stoichiometries as a function of pressure and temperature (Table 1), the unquenchable phase appears to exhibit a general decrease in Mg content with increasing temperature, away from the $MgO+Fe_2O_3$ stability field. However a more precise analysis is precluded by the inherent uncertainties in the pressure and temperature of the individual experiments (see above).

Although the exact nature of the unquenchable phases remains unknown, our experiments at ~10 GPa and above 1200 °C demonstrate that the boundary delineating the $MgFe_2O_4$ breakdown reaction is virtually isobaric (Fig. 3). In situ measurements will be necessary to provide more precise information about the true nature of the Mg-Fe oxides stable above ~10 GPa.

### Stability of $Mg_2Fe_2O_5+Fe_2O_3$

The stability field for the unquenchable phases and hematite is narrow in terms of pressure, giving way to the recoverable assemblage of $Mg_2Fe_2O_5+Fe_2O_3$ (Fig. 3; Table 1). This field was not foreseen by Levy et al. (2004). $Mg_2Fe_2O_5$ is isostructural with $Fe_4O_5$ (Boffa Ballaran et al. 2015) and is easily distinguishable from other phases in X-ray powder diffraction patterns (Fig. 8). The unit-cell parameters are given in Table 5 and are very similar to those published for the Mg-end-member $Mg_2Fe_2O_5$ in Boffa Ballaran et al. (2015). This implies little or only minor reduction of ferric to ferrous iron. The occurrence of large crystals in some samples compared to other assemblages (Figs. 1a and 1b) demonstrates its quenchable nature without any apparent spinodal-like texture. With increasing pressure, $Mg_2Fe_2O_5+Fe_2O_3$ becomes stable to lower temperatures at the expense of $MgO+Fe_2O_3$ indicating this boundary has a negative slope (Fig. 3). The $Mg_2Fe_2O_5+Fe_2O_3$ assemblage is stable up to at least 18 GPa, with additional experiments underway to investigate the full breadth of its stability field.

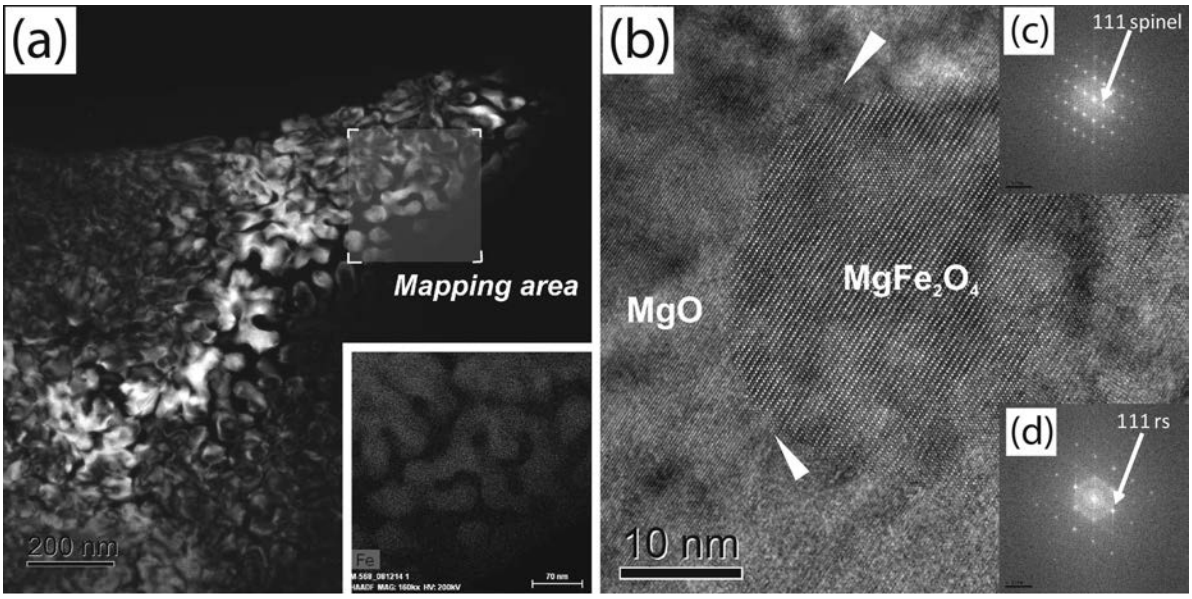


**FIGURE 5.** (**a**) Dark-field TEM image of the unquenchable phase in sample M568, illustrating vermicular intergrowths. The domains with white contrast correspond to Fe-enriched magnesioferrite. The inset is an iron elemental map of the squared area. The STEM-EDX map of Fe concentrations denotes two intimately intergrowth phases with different compositions. (**b**) A high-resolution TEM image of a fine mixture of MgO (periclase) and $MgFe_2O_4$ (magnesioferrite), indicating a topotactic relationship of their lattice fringes of oxygen close-packed planes (white arrow heads). (**c**) Fast Fourier transform (FFT) pattern from image of the Fe-rich domain, indexed as a cubic spinel structure. (**d**) FFT pattern from the Mg-rich domain, indexed as having the rock salt (rs) structure. Some additional diffraction spots, e.g., *d*-spacing of 0.26 nm originate from the Fe-rich domain.

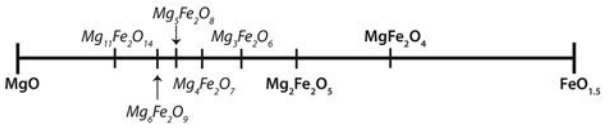


**FIGURE 6.** The MgO-$FeO_{1.5}$ binary with stoichiometries of known and hypothetical phases indicated.

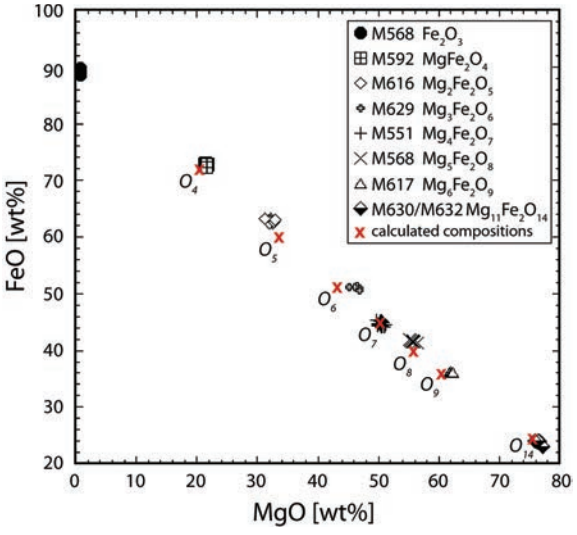


**FIGURE 7.** Chemical compositions of representative run products plotted in terms of their MgO and FeO contents in wt%. Plotted are hematite, magnesioferrite ($O_4$) and $Mg_2Fe_2O_5$ ($O_5$) as quenchable phases and bulk chemical analyses of the unquenchable phases that are consistent with the hypothetical stoichiometries of $Mg_3Fe_2O_6$ ($O_6$), $Mg_4Fe_2O_7$ ($O_7$),$Mg_5Fe_2O_8$ ($O_8$), $Mg_6Fe_2O_9$ ($O_9$), or $Mg_{11}Fe_2O_{14}$ ($O_{14}$). (Color online.)

### High-pressure behavior of hematite

The phase relations of magnesioferrite as depicted in Figure 3 demonstrate that hematite plays an important role in post-spinel assemblages. It occurs with various phases that always have a higher $Mg/Fe^{3+}$ than that present in $MgFe_2O_4$. The coexistence of hematite also implies that no other phases with lower $Mg/Fe^{3+}$ (i.e., a Mg-bearing solid solution of $Fe_{13}O_{19}$; Merlini et al. 2015) are stable within the pressure and temperature range of our experiments. However, at such high pressures the hematite is not pure $Fe_2O_3$, but was found to incorporate up to ~3.5 wt% MgO (≙0.135 cations per formula unit, cpfu). This is not an analytical artifact since we observe Mg contents to increase with increasing temperature of the experiment (Fig. 9a). In addition, the lattice parameters and molar volume systematically change with measured Mg concentration (Table 6; Figs. 9b, 9c, and 9d). The substitution of divalent Mg for $Fe^{3+}$ can be understood in terms of a $Mg_3O_3$ component, where two $Fe^{3+}$ cations are replaced by Mg and an additional Mg cation occupies a normally adjacent vacant site in the crystal structure (Berry et al. 1998, 2000). While $\alpha$-$Fe_2O_3$ has pairs of face-sharing $FeO_6$ octahedra along [001], the incorporation of Mg leads to the formation of triplets along the same crystallographic direction. In this way charge balance is maintained, but stoichiometry deviates from the ideal two cations per three O atoms through the presence of interstitial Mg (Table 6). Our data set is in good agreement with this structural

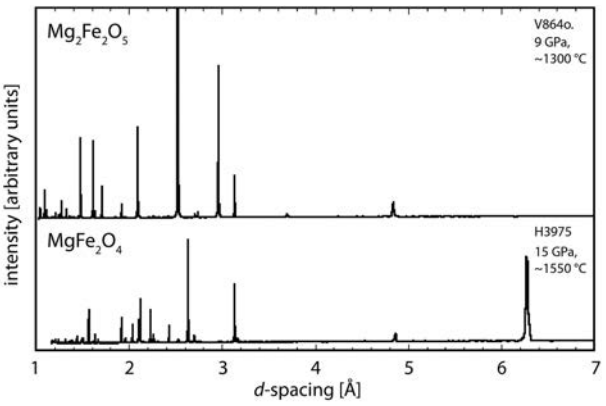


**Figure 8.** Comparison of powder X-ray diffraction patterns of $Mg_2Fe_2O_5$ and $MgFe_2O_4$.

**Table 5.** Unit-cell parameters of $Mg_2Fe_2O_5$

| Sample | *a* (Å) | *b* (Å) | *c* (Å) | *V* (Å$^3$) |
|---|---|---|---|---|
| M616 | 2.8863(16) | 9.730(6) | 12.540(6) | 352.16(20) |
| M617 | 2.8870(4) | 9.7225(15) | 12.5527(15) | 352.34(6) |
| H3889 | 2.8858(2) | 9.7187(9) | 12.5476(9) | 351.91(3) |
| Z1461o | 2.8884(7) | 9.7253(25) | 12.5468(26) | 352.45(9) |
| Z1463o | 2.8872(2) | 9.7228(8) | 12.5523(9) | 352.36(3) |

*Note:* Uncertainties in brackets are those returned by the GSAS refinement.

model in so far as the observed expansion along the *c*-axis is about twice that along the *a*-axis (see Figs. 9c and 9d). The maximum extent of non-stoichiometry reaches 2.045 cations on a three-oxygen basis (Table 6), which should act to stabilize the assemblage hematite + MgO. As a result, we would expect the phase boundary between $MgFe_2O_4$ and this assemblage to shift to lower pressures. However, hematite in this range of pressure and temperature contains less Mg, reaching a maximum non-stoichiometry of 2.019 cations on a three-oxygen basis in sample M588 (Table 6). Assuming that Raoult's law is valid over this small compositional range (mole fraction of hematite = 0.981), we can estimate the effect of solid solution on the position of the phase boundary. In this case, the free energy difference amounts to only several hundred joules, which implies a shift of <0.1 GPa. Thus, this effect cannot account for the observed discrepancy between our results for equilibrium 1 and the calculations of Levy et al. (2004).

### Comparison with other Mg and Fe-bearing oxide systems

Aside from ringwoodite, mantle-derived spinels have major element compositions dominated by Mg and $Fe^{2+}$, along with $Fe^{3+}$, Cr, and/or Al as trivalent cations. Therefore, it is of interest to compare the phase relations in different end-member systems to predict the behavior of more complex solid solutions and to

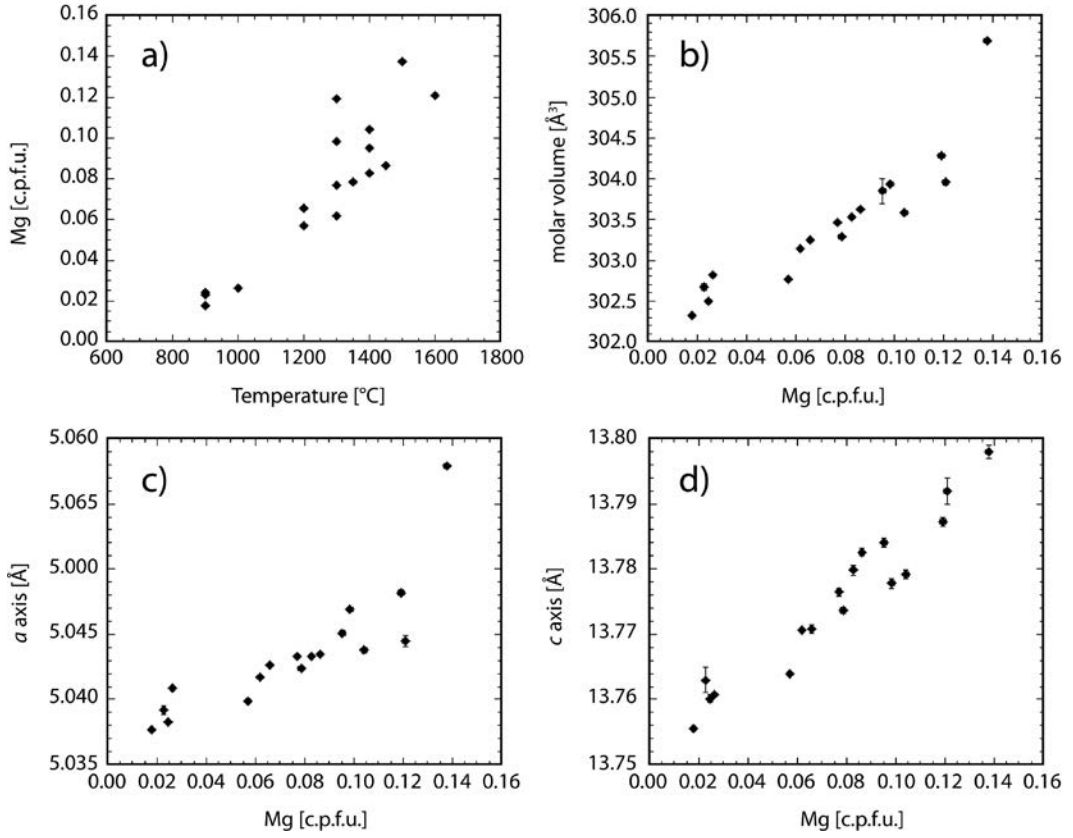


**Figure 9.** (**a**) Variation in Mg content (cations per formula unit, cpfu) in hematite as a function of temperature of the experiment. Systematic variations in molar volume (**b**) and the lattice parameters (**c** and **d**), as a function of measured Mg content in hematite. Error bars represent uncertainties from refinement of the powder diffraction patterns. Where there are no error bars, the errors are about the size of the symbol.

**TABLE 6.** Unit-cell parameters and molar volume of hematite as well as the Mg content in hematite

| Experiment | *a* (Å) | *c* (Å) | *V* (Å$^3$) | Mg content (cpfu) |
|---|---|---|---|---|
| H3889 | 5.0482(2) | 13.7873(7) | 304.284(16) | 0.1191(12) |
| M551 | 5.0579(2) | 13.798(1) | 305.688(28) | 0.1377(12) |
| M573 | 5.0383(1) | 13.7601(6) | 302.496(13) | 0.0243(5) |
| M568 | 5.0451(2) | 13.7841(7) | 303.847(15) | 0.0952(11) |
| M569 | 5.0409(1) | 13.7608(3) | 302.824(7) | 0.0262(6) |
| M577 | 5.0377(1) | 13.7555(3) | 302.326(7) | 0.0177(5) |
| M585 | 5.0392(3) | 13.763(2) | 302.68(4) | 0.0229(5) |
| M588 | 5.0399(1) | 13.7639(3) | 302.767(8) | 0.0571(8) |
| M590 | 5.0426(1) | 13.7708(7) | 303.249(15) | 0.0656(9) |
| M616 | 5.0445(4) | 13.792(2) | 303.96(3) | 0.1208(12) |
| M617 | 5.0433(2) | 13.7798(7) | 303.527(15) | 0.0826(10) |
| M630 | 5.0424(1) | 13.7737(5) | 303.291(11) | 0.0785(10) |
| M631 | 5.0435(1) | 13.7826(6) | 303.622(14) | 0.0862(10) |
| M632 | 5.0433(1) | 13.7765(6) | 303.463(14) | 0.0768(10) |
| V841o | 5.0469(1) | 13.7778(8) | 303.927(17) | 0.0983(11) |
| Z1461o | 5.0418(1) | 13.7707(3) | 303.146(6) | 0.0618(9) |
| Z1463o | 5.0438(2) | 13.7792(7) | 303.580(16) | 0.1041(11) |

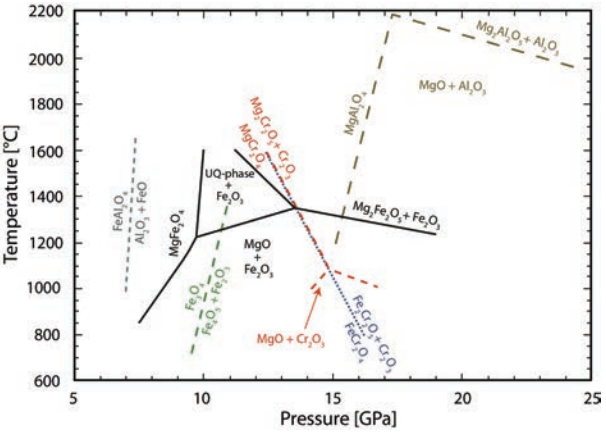


**FIGURE 10.** Comparison of the conditions of the breakdown of spinel-structured phases in several end-member compositions. Stability fields for the constituent oxide and $A_2B_2O_5$+$M_2O_3$ assemblages are also displayed in systems where they are stable. Data sources: hercynite ($FeAl_2O_4$), Schollenbruch et al. (2010); magnetite ($Fe_3O_4$), Woodland et al. (2012); chromite ($FeCr_2O_4$), Ishii et al. (2014); magnesiochromite ($MgCr_2O_4$), Ishii et al. (2015); spinel ($MgAl_2O_4$), Akaogi et al. (1999) and Enomoto et al. (2009). (Color online.)

understand how the incorporation of certain cations may affect phase stabilities. We have demonstrated that the phase relations for $MgFe_2O_4$ are more complicated than proposed by Levy et al. (2004). At about 9 GPa and temperatures up to 1200 °C, $MgFe_2O_4$ breaks down to its constituent oxides: MgO+$Fe_2O_3$. This contrasts with the Mg-free analog $FeFe_2O_4$, where no such field has been observed (Schollenbruch et al. 2011; Huang and Bassett 1986). Instead, magnetite breaks down at 9.5–11 GPa and 700–1400 °C by undergoing a disproportionation reaction to $Fe_4O_5$+$Fe_2O_3$ (Woodland et al. 2012). In the $MgFe_2O_4$ system, $Mg_2Fe_2O_5$+$Fe_2O_3$ does become stable at somewhat higher pressures (Figs. 3 and 10), but magnesioferrite does not directly break down to this assemblage. In this case, there is an intervening field involving one or more unquenchable Mg-Fe oxides that appear to have more complex stoichiometries (see above). Thus, substitution of Mg for $Fe^{2+}$ in the presence of $Fe^{3+}$ does not just lead to a shift in phase boundaries to different pressures and temperatures, but it alters the phase relations by stabilizing additional phase fields. On the other hand, it is notable that the high-pressure stabilities of magnesioferrite and magnetite are similar (they lie within a couple of GPa at a given temperature, see Fig. 10).

In Cr-bearing compositions, phase relations exhibit similarities and differences compared to the $Fe^{3+}$-bearing end-members (Fig. 10). Recent studies on chromite ($FeCr_2O_4$) and magnesiochromite ($MgCr_2O_4$) by Ishii et al. (2014, 2015) also highlight the influence of $Mg^{2+}$ on the phase relations of Cr-spinels. In a fashion analogous to magnetite, chromite breaks down to $Fe_2Cr_2O_5$+$Cr_2O_3$, although $Fe_2Cr_2O_5$ has apparently a slightly different crystal structure than that observed for $Fe_4O_5$. Magnesiochromite reacts directly to $Mg_2Cr_2O_5$+$Cr_2O_3$ (Ishii et al. 2015), without any intermediate phase field, which contrasts with that observed for $MgFe_2O_4$. On the other hand, $MgCr_2O_4$ also breaks down to its constituent oxides at low temperatures, like $MgFe_2O_4$ does. Such a phase field is clearly not favored in $Fe^{2+}$-bearing end-members regardless of whether $Fe^{3+}$ or Cr is the trivalent cation. The high-pressure stability limits of chromite and magnesiochromite are nearly identical [Fig. 10; Ishii et al. (2014, 2015)] and lie 2–5 GPa higher than those for the $Fe^{3+}$-bearing spinel phases.

The Mg-bearing spinel, $MgAl_2O_4$, exhibits different phase relations in that it breaks down to its constituent oxides (MgO+$Al_2O_3$) at 15–16 GPa and over a wide range of temperatures (1000–1600 °C; Liu 1975; Akaogi et al. 1999). At temperatures >1900 °C, Enomoto et al. (2009) reported that MgO+$Al_2O_3$ reacts to form the assemblage $Mg_2Al_2O_5$+$Al_2O_3$ at 20–26 GPa. These relations are not unlike those observed for $MgFe_2O_4$ (Figs. 3 and 10) and $MgCr_2O_4$ (Ishii et al. 2015), albeit with the different phase fields occurring at much higher temperatures. As illustrated in Figure 10, the maximum pressure stabilities of the Mg-bearing spinel-structured phases in their respective systems have the following sequence: $MgAl_2O_4$ > $MgCr_2O_4$ > $MgFe_2O_4$.

The $Fe^{2+}$-bearing analog to spinel, hercynite ($FeAl_2O_4$), disproportionates into a mixture of corundum and wüstite at 7–8.5 GPa and temperatures of 900–1700 °C (Schollenbruch et al. 2010). The constituent oxides remain stable up to at least 24 GPa and 1700 °C, with no evidence for a $Fe_2Al_2O_5$ phase becoming stable. However, considering the results of Enomoto et al. (2009), it is still possible that an assemblage of $Fe_2Al_2O_5$+$Al_2O_3$ might be stable above 1700 °C. Comparison of the $Fe^{2+}$-bearing systems reveals that the sequence of maximum pressure stability for the spinel-structured phases is $FeCr_2O_4$ > $FeFe_2O_4$ > $FeAl_2O_4$, which is quite different from that of the Mg-bearing analogs (Fig. 10).

## IMPLICATIONS FOR THE MANTLE

Studies of inclusions in diamonds provide direct information about the conditions and composition of the Earth's deep interior, at least of the local domain in which a diamond crystallized. For example, inclusions can potentially give evidence for the prevailing pressure, temperature, and, possibly, oxygen fugacity conditions during entrapment. Several studies report various non-silicate inclusions with simple oxide compositions, including magnetite, wüstite, and metallic Fe (e.g., Meyer 1987; Stachel et al. 1998). Their occurrence together in a single diamond emphasizes the fact that diamond formation may take place in a significant redox gradient (Stachel et al. 1998).

Inclusions of (Mg,Fe)O in diamond are often considered to indicate a deep origin in the lower mantle (e.g., Harte et al. 1999). Samples from Juina Province, Brazil, are particularly noteworthy in that the inclusions also contain nanometer-sized magnesioferrite (Harte et al. 1999; Wirth et al. 2014; Kaminsky et al. 2015; Palot et al. 2016). In their TEM study, Wirth et al. (2014) identified platelets of $(Mg_{0.5}Fe_{0.5})Fe_2O_4$ occurring along dislocations or at the diamond-inclusion interface. In addition, magnetite, Al-bearing spinel and a Fe-Ni alloy were also found to occur within the host inclusion. The observed microtextures were interpreted by Wirth et al. (2014) as indicating that $(Mg_{0.5}Fe_{0.5})Fe_2O_4$ originally formed as a high-pressure polymorph that reverted to magnesioferrite during decompression. Palot et al. (2016) also reported magnesioferrite with an approximate composition of $Mg(Fe_{0.75},Cr_{0.17},Al_{0.08})_2O_4$ decorating dislocations and occurring as 10–20 nm euhedral crystals within another (Mg,Fe)O included in diamond from the same location. Based upon a phase diagram valid for 1 atm, they considered this phase to have formed during uplift, but still within the lower mantle at pressures >25 GPa. Furthermore, the occurrence of euhedral precipitates was interpreted as indicating that the magnesioferrite formed directly from the ferropericlase host. However, our phase relations presented in Figures 3 and 10 demonstrate that: (1) magnesioferrite is not stable at such pressures, and (2) magnesioferrite does not directly transform into a high-pressure polymorph, hp-$MgFe_2O_4$ not being stable up to 18 GPa, at least at 1300 °C. Such a hp-$MgFe_2O_4$ phase may be stable at still higher pressures, as reported by Andrault and Bolfan-Casanova (2001). However, there must be an intervening stability field with the assemblage "$O_5$" phase + sesquioxide solid solution (i.e., a $Fe_2O_3$-rich phase) between the fields of magnesioferrite and the high-pressure polymorph. This is also the case for Cr-bearing compositions [Fig. 10; Ishii et al. (2014, 2015)]. It is important to note that Wirth et al. (2014) reported the presence of an additional, unidentifiable phase located between the magnesioferrite platelets, implying that the precursor had a stoichiometry different from that of spinel. An alternative interpretation could be that at transition zone conditions, $Mg_2Fe_2O_5$ initially exsolved from the host (Mg,Fe)O, and during upwelling subsequently reacted to one or other of our unquenchable Mg-Fe oxides (e.g., $Mg_4Fe_2O_7$ or $Mg_5Fe_2O_8$, etc.) before further reacting to magnesioferrite upon reaching its stability field in the upper mantle (i.e., 9–10 GPa).

The presence of magnesioferrite led both Wirth et al. (2014) and Palot et al. (2016) to propose that the original (Mg,Fe)O had a significant non-stoichiometry (i.e., $Fe^{3+}$ content). However, such a degree of non-stoichiometry is inconsistent with experimental data (McCammon et al. 1998). Another possibility is in situ oxidation through reaction with a small amount of carbonate-bearing (fluid or a solid) that was trapped along with the (Mg,Fe)O inclusion. A coupled reaction of the form: 2 FeO (oxide) + $CO_2$ = C + $Fe_2O_3$ (oxide) would produce diamond together with ferric iron that would drive the formation of an additional phase such as $Mg_2Fe_2O_5$. In fact, Palot et al. (2016) report the coexistence of brucite in the host ferropericlase, providing direct evidence for the presence of a fluid. Carbonate inclusions have been reported in other diamonds from the same locality (Kaminsky et al. 2009, 2013), further supporting this possibility.

The mechanism of carbon-iron redox-coupling to produce diamond along with a coexisting $Fe^{3+}$-bearing phase does not have to be restricted to isolated inclusions, but can also have relevance for the diamond-formation process in general. Although they are not expected to be stable at the ambient oxidation state of the transition zone (i.e., near metal saturation, Frost and McCammon 2008), such $Fe^{3+}$-rich phases can develop locally where strong redox gradients attend diamond formation (Stachel et al. 1998). On the other hand, the many similarities between $MgFe_2O_4$ and other $AB_2O_4$ end-member systems (where A and B stand for divalent and trivalent cations, respectively) suggest phases like $A_2B_2O_5$ can form complex solid solutions involving trivalent cations other than $Fe^{3+}$. Such substitutions can act to expand the redox stability of these phases. So far unique to $MgFe_2O_4$ is the occurrence of Mg-Fe oxides with more complex stoichiometries like $Mg_4Fe_2O_7$ or $Mg_5Fe_2O_8$, or even $Mg_{11}Fe_2O_{14}$. Whether these phases can also form solid solutions awaits further study. Although $Fe_5O_6$ has been reported (Lavina and Meng 2015; Woodland et al. 2015), it is not a stable phase in a $Fe_3O_4$ bulk composition (Woodland et al. 2015). Interestingly, one of the unquenchable phases encountered at 10 GPa and 1500 °C had a $Mg_3Fe_2O_6$ stoichiometry, which would represent an analog to $Fe_5O_6$ (Table 1). Whether this Mg-end-member has a large stability field (or is quenchable) in more Mg-rich bulk compositions remains to be investigated.

Magnesioferrite and magnetite have very similar high-pressure stabilities, both breaking down at 9–10 GPa (Schollenbruch et al. 2011; Woodland et al. 2012). Although the phase relations of magnetite have received much attention over the years, no additional oxide phases with stoichiometries of, e.g., $Mg_4Fe_2O_7$ or $Mg_5Fe_2O_8$, have been reported. The high-pressure and high-temperature behavior of solid solutions along the $MgFe_2O_4$–$FeFe_2O_4$ could be of further interest, in that their composition is more applicable for the Earth's mantle. Thus, an experimental study on the phase relations of $(Mg_{0.5}Fe_{0.5})Fe_2O_4$ similar to that identified by Wirth et al. (2014) in their ferropericlase inclusion is currently underway.

## Acknowledgments

This work was supported by the Deutsche Forschungsgemeinschaft through grants WO 652/20-1 and BO 2550/7-1 to A.B.W. and T.B.B., respectively. E. Alig and H. Höfer are thanked for helping with the X-ray powder diffraction and microprobe measurements, respectively. The manuscript was improved through insightful comments from R. Myhill and an anonymous reviewer. Fruitful discussions with R. Angel and F. Brenker are gratefully acknowledged.

## References cited

Akaogi, M., Hamada, Y., Suzuki, T., Kobayashi, M., and Okada, M. (1999) High pressure transitions in the system $MgAl_2O_4$–$CaAl_2O_4$: A new hexagonal aluminous phase with implication for the lower mantle. Physics of the Earth and Planetary Interiors, 115, 67–77.

Andrault, D., and Bolfan-Casanova, N. (2001) High-pressure phase transformations in the $MgFe_2O_4$ and $Fe_2O_3$-$MgSiO_3$ systems. Physics and Chemistry of Minerals, 28, 211–217.

Armstrong, J.T. (1993) Matrix correction program CITZAF, ver. 3.5. California Institute of Technology.

Berry, F.J., Bohorquez, A., Greaves, C., McManus, J., Moore, E.A., and Mortimer, M. (1998) Structural characterization of divalent magnesium-doped $\alpha$-$Fe_2O_3$. Journal of Solid State Chemistry, 140, 428–430.

Berry, F.J., Greaves, C., Helgason, Ö., McManus, J., Palmer, H.M., and Williams, R.T. (2000) Structural and magnetic properties of Sn-, Ti-, and Mg-substituted $\alpha$-$Fe_2O_3$: A study by neutron diffraction and Mössbauer spectroscopy. Journal of Solid State Chemistry, 151, 157–162.

Boffa Ballaran, T., Uenver-Thiele, L., Woodland, A.B., and Frost, D.J. (2015) Complete substitution of $Fe^{2+}$ by Mg in $Fe_4O_5$: The crystal structure of the $Mg_2Fe_2O_5$ end-member. American Mineralogist, 100, 628–632.

Brey, G., Bulatov, V., and Girnis, A. (2008) Geobarometry for peridotites: Experiments in simple and natural systems from 6 to 10 GPa. Journal of Petrology, 49, 3–24.

Enomoto, A., Kojitani, H., Akaogi, M., Miura, H., and Yusa, H. (2009) High-pressure transitions in $MgAl_2O_4$ and a new high-pressure phase of $Mg_2Al_2O_5$. Journal of Solid State Chemistry, 182, 389–395.

Frost, D.J., and McCammon, C.A. (2008) The redox state of Earth's mantle. Annual Reviews of Earth and Planetary Sciences, 36, 389–420, doi:10.1146/Annurev.Earth.36.031207.124322.

Harte, B., Harris, J.W., Hutchison, M.T., Watt, G.R., and Wilding, M.C. (1999) Lower mantle mineral associations in diamonds from São Luiz, Brazil. In F.R. Boyd, Y. Fei, C.M. Bertka, and B.O. Mysen, Eds., Mantle Petrology: Field observations and high pressure experimentation. The Geochemical Society, Special Publication, 6, 125–153.

Hazen, R.M. (1976) Effects of temperature and pressure on the cell dimension and X-ray temperature factors of periclase. American Mineralogist, 61, 266–271.

Holland, T.J.B., and Powell, R. (2011) An improved and extended internally consistent thermodynamic dataset for phases of petrological interest, involving a new equation of state for solids. Journal of Metamorphic Geology, 29, 333–383.

Huang, E., and Bassett, W.A. (1986) Rapid-determination of $Fe_3O_4$ phase-diagram by synchrotron radiation. Journal of Geophysical Research, 91(B5), 4697–4703.

Ishii, T., Kojitani, H., Tsukamoto, S., Fujino, K., Mori, D., Inaguma, Y., Tsujino, N., Yoshino, T., Yamazaki, D., Higo, Y., Funakoshi, K., and Akaogi, M. (2014) High-pressure phase transitions in $FeCr_2O_4$ and structure analysis of new post-spinel $FeCr_2O_4$ and $Fe_2Cr_2O_5$ phases with meteoritical and petrological implications. American Mineralogist, 99, 1788–1797.

Ishii, T., Kojitani, H., Fujino, K., Yusa, H., Mori, D., Inaguma, Y., Matsushita, Y., Yamaura, K., and Akaogi, M. (2015) High-pressure high-temperature transitions in $MgCr_2O_4$ and crystal structures of new $Mg_2Cr_2O_5$ and post-spinel $MgCr_2O_4$ phases with implications for ultrahigh-pressure chromitites in ophiolites. American Mineralogist, 100, 59–65.

Kaminsky, F., Wirth, R., Matsyuk, S., Schreiber, A., and Thomas, R. (2009) Nyerereite and nahcolite inclusions in diamond: evidence for lower-mantle carbonatitic magmas. Mineralogical Magazine, 73, 5, 797–816.

Kaminsky, F.V., Wirth, R., and Schreiber, A. (2013) Carbonatitic inclusions in deep mantle diamond from Juina, Brazil: New minerals in the carbonate-halide association. Canadian Mineralogist, 51, 669–688.

Kaminsky, F.V., Ryabchikov, I.D., McCammon, C.A., Longo, M., Abakumov, A.M., Turnerd, S., and Heidari, H. (2015) Oxidation potential in the Earth's lower mantle as recorded by ferropericlase inclusions in diamond. Earth and Planetary Science Letters, 417, 49–56.

Keppler, H., and Frost, D.J. (2005) Introduction to minerals under extreme conditions. In R. Miletich, Ed., Mineral Behaviour at Extreme Conditions. EMU Notes in Mineralogy, 7, 1–30.

Kyono, A., Gramsch, S.A., Yamanaka, T., Ikuta, D., Ahart, M., Mysen, B.O., Mao, H., and Hemley, R.J. (2012) The influence of the Jahn-Teller effect at $Fe^{2+}$ on the structure of chromite at high pressure. Physics and Chemistry of Minerals, 39, 131–141.

Larson, A.C., and von Dreele, R.B. (1994) GSAS General Structure Analysis System. Los Alamo National Laboratory, New Mexico, U.S.A.

Lavina, B., and Meng, Y. (2015) Unraveling the complexity of iron oxides at high pressure and temperature: Synthesis of $Fe_5O_6$. Science Advances 1, e1400260.

Lavina, B., Dera, P., Kim, E., Meng, Y., Downs, R.T., Weck, P.F., Sutton, S.R., and Zhao, Y. (2011) Discovery of the recoverable high-pressure iron oxide $Fe_4O_5$. Proceedings of the National Academy of Sciences, 108, 17281–17285.

Levy, D., Diella, V., Dapiaggi, M., Sani, A., Gemmi, M., and Pavese, A. (2004) Equation of state, structural behaviour and phase diagram of synthetic $MgFe_2O_4$, as a function of pressure and temperature. Physics and Chemistry of Minerals, 31, 122–129.

Liu, L.G. (1975) Disproportionation of $MgAl_2O_4$ spinel at high-pressure and temperature. Geophysical Research Letters, 2, 9–11.

McCammon, C., Peyronneau, J., and Poirier, J.-P. (1998) Low ferric iron content of (Mg,Fe)O at high pressures and temperatures. Geophysical Research Letters, 25, 1589–1592.

Merlini, M., Hanfland, M., Salamat, A., Petitgirard, S., and Müller, H. (2015) The crystal structures of $Mg_2Fe_2C_4O_{13}$, with tetrahedrally coordinated carbon, and $Fe_{13}O_{19}$, synthesized at deep mantle conditions. American Mineralogist, 100, 2001–2004.

Meyer, H.O.A. (1987) Inclusions in diamond. In P.H. Nixon, Ed., Mantle Xenoliths, p. 501–523. Wiley, New York.

Myhill, B., Ojwang, D.O., Ziberna, L., Frost, D., Boffa Ballaran, T., and Miyamjima, N. (2016) On the *P-T-*$f_{O_2}$ stability of $Fe_4O_5$ and $Fe_5O_6$-rich phases: A thermodynamic and experimental study. Contributions to Mineralogy and Petrology, 171, 5, 1–11.

O'Neill, H.St.C., Annersten, H., and Virgo, D. (1992) The temperature dependence of the cation distribution of magnesioferrite ($MgFe_2O_4$) from powder XRD structural refinements and Mössbauer spectroscopy. American Mineralogist, 77, 725–740.

Ono, S., Kikegawa, T., and Ohishi, Y. (2006) The stability and compressibility of $MgAl_2O_4$ high-pressure polymorphs. Physics and Chemistry of Minerals, 33, 200–206.

Palot, M., Jacobsen, S.D., Townsend, J.P., Nestola, F., Marquardt, K., Miyajima, N., Harris, J.W., Stachel, T., McCammon, C.A., and Pearson, D.G. (2016) Evidence for $H_2O$-bearing fluids in the lower mantle from diamond inclusion. Lithos, 265, 237–243.

Schollenbruch, K., Woodland, A.B., and Frost, D.J. (2010) The stability of hercynite at high pressures and temperatures. Physics and Chemistry of Minerals, 37, 137–143.

Schollenbruch, K., Woodland, A.B., Frost, D.J., Wang, Y., Sanehira, T., and Langenhorst, F. (2011) In situ determination of the spinel–post-spinel transition in $Fe_3O_4$ at high pressure and temperature by synchrotron X-ray diffraction. American Mineralogist, 96, 820–827.

Stachel, T., Harris, J.W., and Brey, G.P. (1998) Rare and unusal mineral inclusions in diamonds from Mwadui, Tanzania. Contributions to Mineralogy and Petrology, 132, 34–47.

Toby, B.H. (2001) EXPGUI, a graphical user interface for GSAS. Journal of Applied Crystallography, 34, 210–213.

Walker, D., Carpenter, M.A., and Hitch, C.M. (1990) Some simplifications to multianvil devices for high pressure experiments. American Mineralogist, 75, 1020–1028.

Wang, Z., Downs, R.T., Pischedda, V., Shetty, R., Saxena, S.K., Zha, C.S., Zhao, Y.S., Schiferl, D., and Waskowska, A. (2003) High-pressure X-ray diffraction and Raman spectroscopic studies of the tetragonal spinel $CoFe_2O_4$. Physical Review B, 68, 094101.

Wirth, R., Dobrzhinetskay, L., Harte, B., Schreiber, A., and Green, H.W. (2014) High-Fe (Mg,Fe)O inclusion in diamond apparently from the lowermost mantle. Earth and Planetary Science Letters, 404, 365–375.

Woodland, A.B., Frost, D.J., Trots, D.M., Klimm, K., and Mezouar, M. (2012) In situ observation of the breakdown of magnetite ($Fe_3O_4$) to $Fe_4O_5$ and hematite at high pressures and temperatures. American Mineralogist, 97, 1808–1811.

Woodland A., Uenver-Thiele, L., and Boffa Ballaran, T. (2015) Synthesis of $Fe_5O_6$ and the high-pressure stability of $Fe^{2+}$-$Fe^{3+}$-oxides related to $Fe_4O_5$. Goldschmidt Abstracts, 3446.

Yamanaka, T., Uchida, A., and Nakamoto, Y. (2008) Structural transition of post-spinel phases $CaMn_2O_4$, $CaFe_2O_4$, and $CaTi_2O_4$ under high pressures up to 80 GPa. American Mineralogist, 93, 1874–1881.

Yong, W., Botis, S., Shieh, S.R., Shi, W., and Withers, A.C. (2012) Pressure-induced phase transition study of magnesiochromite ($MgCr_2O_4$) by Raman spectroscopy and X-ray diffraction. Physics of the Earth and Planetary Interiors, 196-197, 75–82.

Manuscript received June 3, 2016
Manuscript accepted October 4, 2016
Manuscript handled by Katherine Crispin